Reductant-Activated, High-Coverage, Covalent Functionalization of 1T′-MoS_2

Supporting Information

Ellen X. Yan, Miguel Cabán-Acevedo, Kimberly M. Papadantonakis, Bruce S. Brunschwig, and Nathan S. Lewis

Division of Chemistry and Chemical Engineering, California Institute of Technology, Pasadena, California 91125, United States

Table of Contents

I. General Information

All organic solvents and reagents were purchased commercially and used as received without further purification. Molybdenum disulfide powder (99%), bis(cyclopentadienyl)nickel(II) (nickelocene), and bis(tetramethylcyclopentadienyl)nickel(II) (octamethylnickelocene) were purchased from Alfa Aesar. Anhydrous organic solvents, *n*-butyllithium (1.6 M in hexanes), and bis(cyclopentadienyl)cobalt(II) (cobaltocene) were purchased from Sigma-Aldrich. All of the above chemicals were stored in an Ar-filled glovebox (<1 ppm O_2). Nanopure water with a resistivity of ≥ 18.2 MΩ·cm was obtained from a Barnstead E-Pure system. The centrifuge used for purification was a Beckman Coulter Avanti J-20 XP centrifuge with a JA-17 fixed rotor, where $rcf(\times g) = 137.75 \times (rpm/1000)^2$.

X-ray photoelectron spectroscopy (XPS) and ultraviolet photoelectron spectroscopy (UPS) data were collected using a Kratos AXIS Ultra spectrometer equipped with a hybrid magnetic and electrostatic electron lens system and a delay-line detector (DLD). The photoelectron-ejection vector was 90° with respect to the sample surface plane. XPS data were collected using a monochromatic Al Kα X-ray source (1486.7 eV) at pressures < 9×10^{-9} Torr. The electron-collection lens aperture was set to sample a 700 × 300 μm spot, and the analyzer pass energy was 80 eV for survey spectra and 10 eV for high-resolution spectra. UPS data were collected using a He I ultraviolet source (21.2 eV) at a pressure of 1×10^{-8} Torr in the analysis chamber. The electron-collection lens aperture was set to a 55 μm spot size and the analyzer pass energy was 5 eV. The instrument energy scale and work function were calibrated using clean Au, Ag, and Cu standards. The instrument was operated by Vision Manager software v. 2.2.10 revision 5 and data were analyzed using CasaXPS software (CASA Software Ltd).

Attenuated total reflectance Fourier transform infrared spectroscopy (ATR-FTIR) data were collected using a Thermo Scientific Nicolet 6700 optical spectrometer with a IR6118 Diamond ATR Smart iTR accessory. The spectrometer was equipped with a deuterated L-alanine-doped triglycine sulfate (DLaTGS) detector, an electronically temperature-controlled (ETC) EverGlo mid-IR source, a N_2(g) purge, and a KBr beam splitter. The spectra reported herein are averages of 1000 scans at 2 cm^{-1} resolution, background corrected using the spectrum of *ce*MoS_2. Spectra were collected and processed using OMNIC software v. 9.2.41.

Raman spectra were collected with a Renishaw inVia Raman microprobe equipped with a Leica DM 2500 M microscope, a Leica N Plan 50x objective (numerical aperture = 0.75), a 1800 lines mm^{-1} grating, and a CCD detector configured in a 180° backscatter geometry. A 532 nm diode-pumped solid-state (DPSS) laser (Renishaw RL532C50) was used as the excitation source. A λ/4 plate was used to circularly polarize the incident excitation. No polarizing collection optic was used.

The solid-state carbon-13 (125.4 MHz) nuclear magnetic resonance (NMR) spectra were acquired on a Bruker DSX-500 MHz NMR spectrometer using a Bruker 4.0 mm magic-angle spinning probe at ambient conditions. Samples were prepared by carefully packing dried functionalized MoS_2 powder in a zirconium rotor. For ^{13}C cross-polarization magic angle spinning (^{13}C CPMAS) NMR experiments, 8.0 kHz spin rate, 4 s recycle delay, 2 ms contact time, π/2 pulse width of 4 μs, and typically 4000 scans using a TPPI ^1H decoupling method were used. The spectra were referenced to tetramethylsilane (TMS).

A Cahn C-35 microbalance having a sensitivity of 10 μg was used to determine the concentration of MoS_2 dispersions.

II. Synthetic Methods

1. Synthesis of chemically exfoliated MoS_2 (*ce*MoS_2)

To intercalate Li, MoS_2 powder (400 mg) was heated with *n*-butyllithium (1.6 M in hexanes, 4 mL) for 46 hours in a sealed glass tube. The powder was filtered and washed with anhydrous hexanes (10 × 2 mL), then exfoliated in 180 mL of H_2O. The dispersion was sonicated for 1 h, then centrifuged at 2000 rpm (551 rcf (×g)) for 5 min to remove unexfoliated material. The supernatant was retained and washed twice with H_2O, and optionally washed with anhydrous DMF (N, N-dimethylformamide) for reactions conducted in DMF. The final precipitate was resuspended in either 2:1 water/isopropanol or DMF, depending on the reaction. Samples of *ce*MoS_2 were dropcast from 1:1 water/methanol onto p^+-Si for XPS measurements, and were dried in *vacuo* for 2 days for ATR-FTIR and NMR measurements.

2. Synthesis of functionalized 1T′-MoS_2

Exfoliated MoS_2 was suspended in either 2:1 water/isopropanol or DMF at a concentration of 2 mg/mL in a 20 mL scintillation vial (typically 10 mL). The concentration was determined by evaporating 0.1 mL of solution and measuring the mass using a microbalance. All of the functionalized MoS_2 (fct-MoS_2) samples were synthesized using DMF as the solvent unless otherwise indicated. The alkyl halide was added (10 eq.) and the solution was stirred for 42 h while being covered in aluminum foil. Centrifugation to wash the fct-MoS_2 was performed at 6000 rpm (4959 rcf (×g)) for 30 min rounds, and the precipitate was resuspended by sonication. in between rounds. The product was washed sequentially with isopropanol (3 × 12 mL), methanol (2 × 12 mL), and water (1 × 12 mL). The final product was resuspended in 1:1 water/methanol for dropcasting (XPS) and the solvent was removed in *vacuo* to obtain a dry powder.

3. Reductant-activated functionalization of 1T′-MoS_2

Functionalized MoS_2 was suspended in DMF (10 mL) and the alkyl halide was added (10 eq.). Metallocenes were then added in either ambient conditions (ferrocene) or in an Ar-purged glovebox (nickelocene, octamethylnickelocene, cobaltocene) after purging the MoS_2/DMF solution with Ar(g). The solution was covered with aluminum foil and stirred for 66 h, then purified by centrifugation at 6500 rpm (5820 rcf (×g)) in 10 min rounds, resuspending the precipitate by sonication in between rounds. The product was washed with DMF until the metallocene color was not visible (typically 3-4 rounds × 12 mL), then with isopropanol (2 × 12 mL), and methanol (2 × 12 mL). The final product was resuspended in 1:1 water/methanol for dropcasting (XPS) and the solvent was removed in *vacuo* to obtain a dry powder.

III. Calculations

1. Analysis and quantification of coverage from XPS data

High-resolution XPS data were analyzed using CasaXPS software v. 2.3.17. A Shirley background was applied to all C 1*s*, S 2*p*, and Mo 3*d* spectra, with endpoints averaged from 21 points. Spectra were calibrated by setting the C 1*s* peak at 284.8 eV. Peaks were fitted according to the constraints listed below, and the coverage per sulfur atom was obtained using the area of the functionalized sulfur peaks divided by the total area of all sulfur peaks. This value was doubled to obtain the

coverage per MoS_2 unit. Although a similar value can be obtained by quantifying the sulfur peaks relative to the Mo 3*d* peaks, a comparison within the same XPS binding energy region removes errors associated with any changes in the inelastic mean free path (IMFP) of photoelectrons as the kinetic energy is changed.

Lineshapes

The Mo 3*d* peaks were fit using a modified Lorentzian asymmetric lineshape with tail damping, LF(α, β, *w*, *m*), where α and β determine the tail asymmetry, *w* is the tail damping parameter, and *m* defines the width of the Gaussian. LF(1,1,55,260) was used to fit all Mo 3d peaks based on previous reports modeling Mo XPS peaks.[1] The S 2*s* peak was fit using a Lorentzian asymmetric lineshape, LA(α, β, *m*), with parameters LA(2,2,50) by matching the experimental data and minimizing the residual standard deviation (residual STD) between the fit and the data in CasaXPS. S 2*p* peaks were fit using a Voigt GL(30) function with 70% Gaussian and 30% Lorentzian character, which resulted in a minimum in the residual STD.

Constraints

Due to spin-orbit coupling, the Mo 3*d* and S 2*p* peaks are doublets with specific area ratios and position constraints. The following constraints were placed on the Mo $3d_{3/2}$ peak relative to the Mo$3d_{5/2}$ peak: area($3d_{5/2}$) × 0.67, FWHM($3d_{5/2}$) ± 0.2, and position($3d_{5/2}$) + 3.13 eV. The S $2p_{1/2}$ peaks were fit with the following constraints: area ($2p_{1/2}$) = area($2p_{3/2}$) × 0.5, FWHM equal to that of the $2p_{3/2}$ peak, and position($2p_{3/2}$) + 1.18 eV. In addition, the ratios of the areas and positions of the 2H- to 1T′-MoS_2 S 2*p* peaks was determined from 4 samples of *ce*MoS_2 and used to constrain the ratios of 2H to 1T′-MoS_2 in the analysis of functionalized samples to minimize over- or under-fitting the functionalized sulfur peak. Thus, the 2H-MoS_2 S 2*p* peak areas were constrained to be 18% of the total S 2*p* area in fct-MoS_2 spectra (similar ratio constraint for the Mo 3*d* spectra), and the peak position equal to 1T′-MoS_2 + 1.32 eV. By the same reasoning for consistency, the S* peak was constrained to be 1T′-MoS_2 - 0.7 eV.

Error Analysis

A residual STD close to 1 (~0.97) was observed in the noise of the background in spectra, therefore Poisson statistics can be applied. Since we can assume Poisson distribution for the noise, Monte Carlo simulation can be used to estimate the errors in the fitting and test the reproducibility of the fitting given the constraints above. We applied Monte Carlo simulations using $n = 400$ for number of simulations for all the data used in Figure 4 and found that the mean of the percent standard deviation (%std) of the peak areas was within 2% for all cases except those of chloropropane where functionalization cannot be detected, resulting in an expected larger percentage error (Figure S13). Therefore, our fitting parameters are relatively robust.

2. Quantification of coverage from ^{13}C MAS NMR data

For quantification to corroborate the XPS analysis, solid state magic angle spinning (MAS) ^{13}C NMR spectra was obtained for ^{13}C-enriched methyl-MoS_2 synthesized from ^{13}C-iodomethane under three conditions: no reductant, with nickelocene, and with cobaltocene. Spectra were normalized using an external standard, 1,2,4,5-tetramethyl-1H-imidazole, and corrected for the natural abundance of ^{13}C. The mmol/g of carbon was calculated per sample according to the

standard spectrum, and converted to coverage per MoS_2 using the expected molecular weight of the functionalized samples based on the XPS data (i.e. for no reductant, with ~ 40% coverage per MoS_2, the molecular weight of $MoS_2(^{13}CH_3)_{0.4}$ was used). For example, with 2.4 mmol/g of carbon in the "no reductant" condition and 10.1 mg of sample during the measurement:

coverage per MoS_2 = (mmol of carbon) / (mmol of Mo)
= (2.4 mmol/g × 0.0101 g) / (0.0101 g / (166.5 g/mol) × 1000 mg/g)
= 0.02424 mmol C / 0.06066 mmol Mo
= 0.40

3. Work functions of MoS_2

Work functions for the various compounds were calculated by fitting the high-binding energy cutoff in the UPS spectra for *ce*MoS_2, methyl-MoS_2, and propyl-MoS_2 synthesized from iodomethane and iodopropane for the latter two. The cutoff value was then used to calculate the work function using the formula WF = E(He I) – BE(cutoff) = 21.2 eV – BE(cutoff). Values reported in Figure S8 are the mean of 3 samples ± standard deviation.

4. Effective reduction potential for one-electron reductants

The standard potential for the one-electron redox couple corresponding to each of the reductants used in our experiments was obtained from literature using values obtained in acetonitrile but shifted by +30 mV based on the difference in formal potentials for the ferrocenium/ ferrocene redox couple in acetonitrile vs DMF.[2-3] This conversion affects only the comparison between the MoS_2 work function and the reductant on the absolute energy scale, for which we used E_{vac} = -4.44 V vs SHE, $E(Fc^{+/0})$ = 0.544 V vs Ag/AgCl/KCl(sat'd),[3] and E(Ag/AgCl/KCl(sat'd)) = 0.20 V vs SHE, resulting in an overall of $E(Fc^{+/0})$ = 5.18 V vs E_{vac}. The effective reduction potential for a solution where only the reductant was added was estimated from the Nernst equation assuming a 50:1 ratio of reductant to oxidant (i.e. 98% purity), resulting in a correction of -0.1 V to obtain the effective potentials in Figure 4 and Table S2.

$$E_{\text{eff}} = E(\text{A/A}^-) - \frac{RT}{zF}\ln\frac{a_{\text{Red}}}{a_{\text{Ox}}}$$

IV. Figures

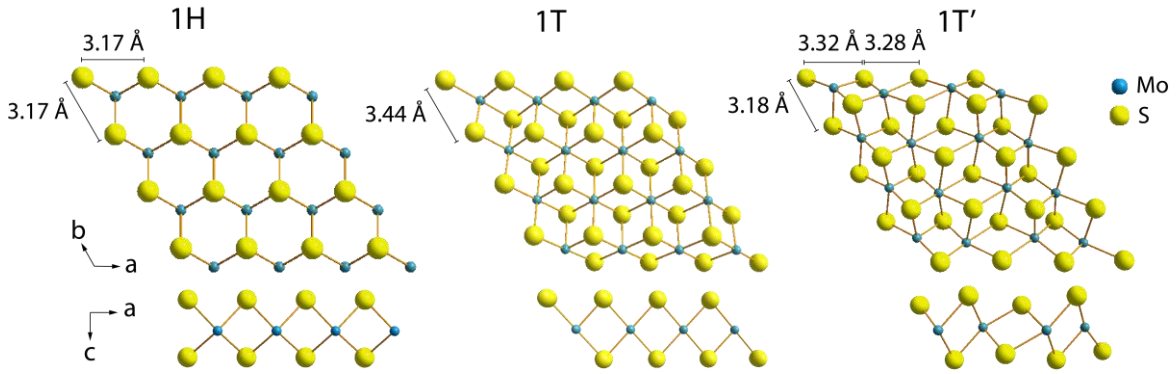

Figure S1. Top-down and side views of 2H-, 1T-, and 1T′-MoS_2. Structures of the 2H and 1T′ phases were generated from crystallographic data,[4-5] and dimensions for the 1T phase obtained from theoretical modeling.[6]

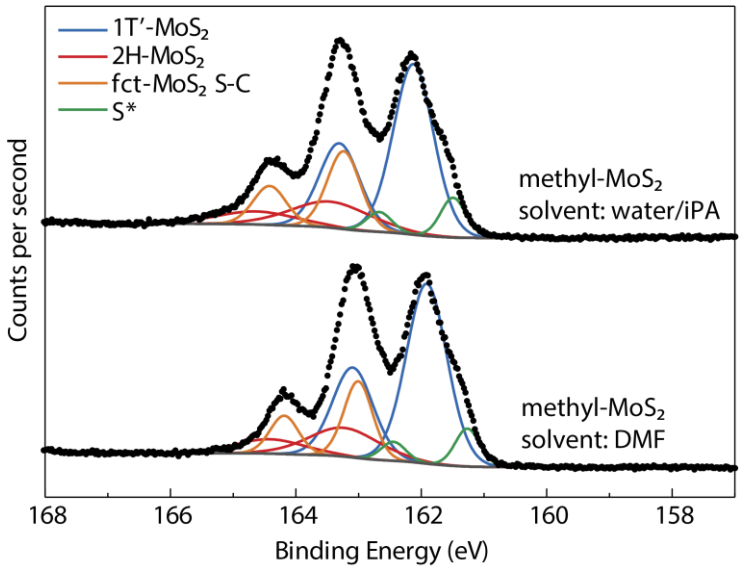

Figure S2. High-resolution XPS of the S 2*p* region for methyl-MoS_2 synthesized from iodomethane either in a 2:1 water/isopropanol solvent (top) or in *N*,*N*-dimethylformamide (DMF) (bottom). No substantial differences were observed between the two spectra.

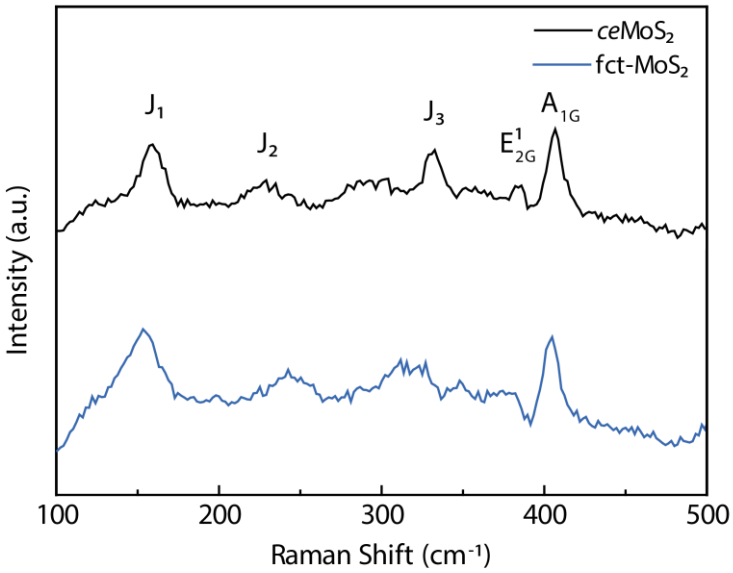

Figure S3. Raman spectra for chemically exfoliated MoS_2 before (top black) and after (bottom blue) functionalization. Characteristic peaks at ~ 159 cm^{-1}, 229 cm^{-1}, and 329 cm^{-1} for the J_1, J_2, and J_3 vibrational modes are consistent with previously reported values for *ce*MoS_2 and demonstrate that the phase is largely unchanged before and after functionalization.[7]

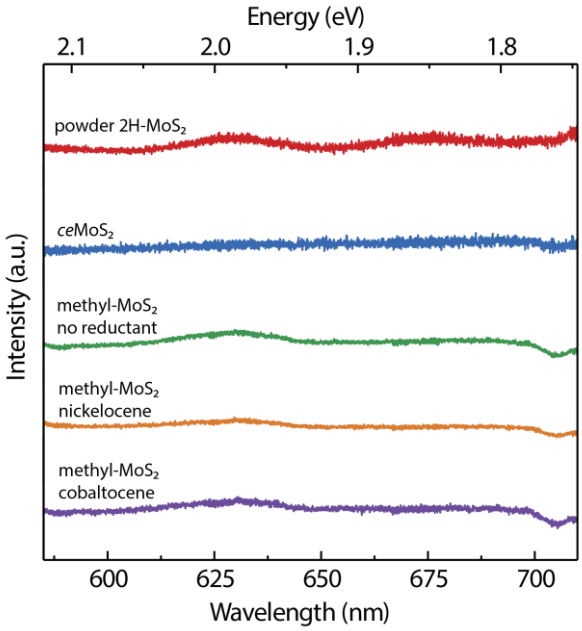

Figure S4. Emission spectra showing photoluminescence region of powder 2H-MoS_2 starting material, chemically exfoliated MoS_2, and functionalized MoS_2 for methyl-MoS_2 synthesized without reductant, with nickelocene, and with cobaltocene. Excitation was from a 532 nm diode pumped solid-state laser. Weak to no photoluminescence is observed before or after functionalization in the region where photoluminescence from mono/few-layer MoS_2 has typically been observed,[8] due to the defect-rich nature of the powdered 2H-MoS_2 starting material.

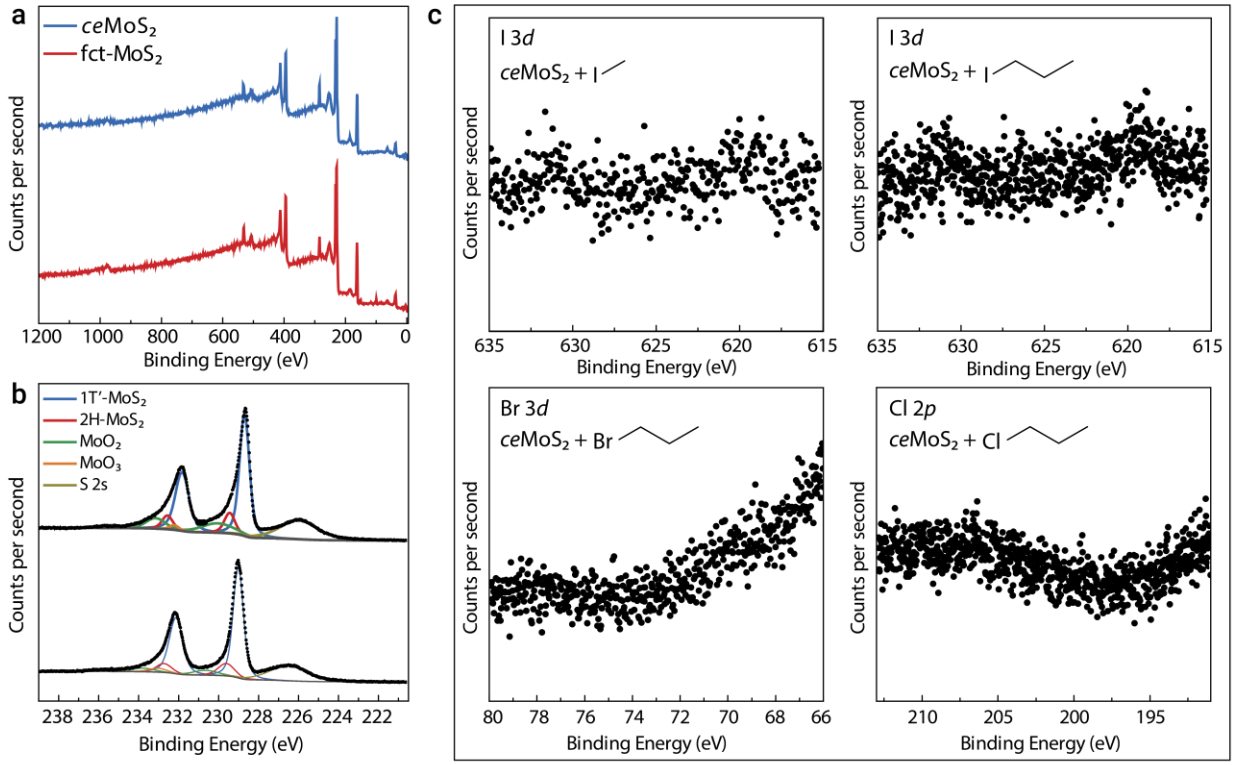

Figure S5. (a) XPS survey and (b) high-resolution XPS of Mo 3*d* region for *ce*MoS_2 and for functionalized MoS_2. No substantial differences were observed between the two spectra. (c) High-resolution XPS data for the halide region of the functionalization molecule (I 3*d*, Br 3*d*, or Cl 2*p*).

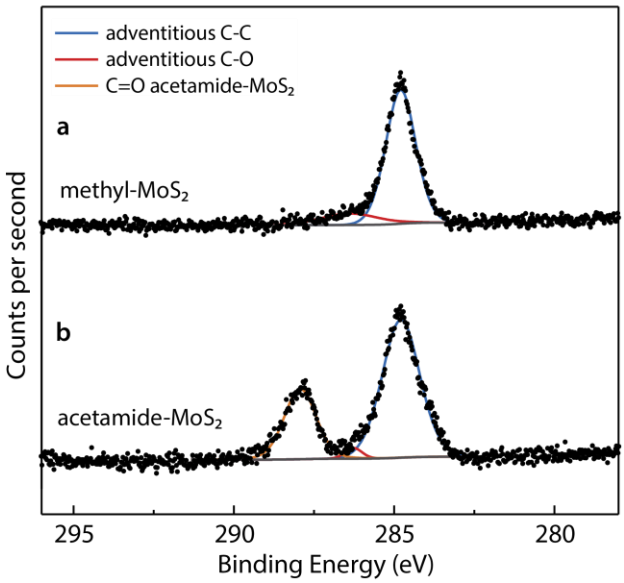

Figure S6. High-resolution XPS of C 1*s* region for (a) functionalized methyl-MoS_2 and (b) functionalized acetamide-MoS_2. Carbon from the carbonyl group is visible in the latter case but not in the former due to overlap with the adventitious carbon peak. The latter result is consistent with previously reported XPS spectra for acetamide-MoS_2.[7]

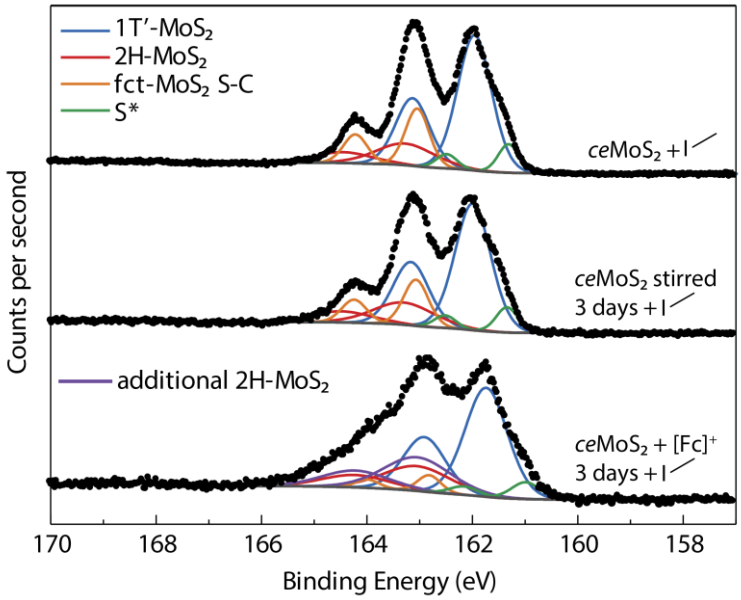

Figure S7. High-resolution XPS of S 2*p* region for (a) *ce*MoS_2 functionalized with iodomethane following the functionalization procedure from the experimental section, (b) *ce*MoS_2 functionalized with iodomethane after stirring for 3 days under ambient conditions, and (c) *ce*MoS_2 stirred for 3 days with ferrocenium tetrafluoroborate ($[Fe(C_5H_5)_2]BF_4$) then functionalized with iodomethane. No substantial differences were observed between the first and second conditions. Spectra of samples functionalized after oxidation of *ce*MoS_2 with ferrocenium (c) exhibited S 2*p* regions with a decreased amount of functionalization and increased amount of 2H-MoS_2 relative to spectra (a) or (b).

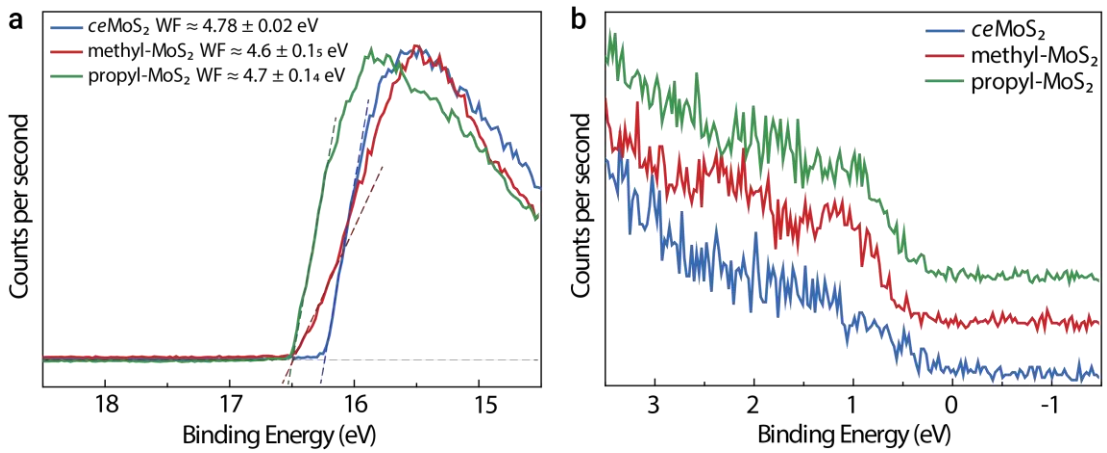

Figure S8. Ultraviolet photoelectron spectra (UPS) for exfoliated MoS_2, methyl-MoS_2, and propyl-MoS_2 synthesized using iodomethane and iodopropane, respectively. (a) The high-binding-energy cut-off used to obtain the work function for these powders. Displayed work function and error range is the average of three samples and the standard deviation. (b) Valence-band regime for the same samples, showing a ≤ 0.3 eV band gap, consistent with theoretical calculations.[9-10]

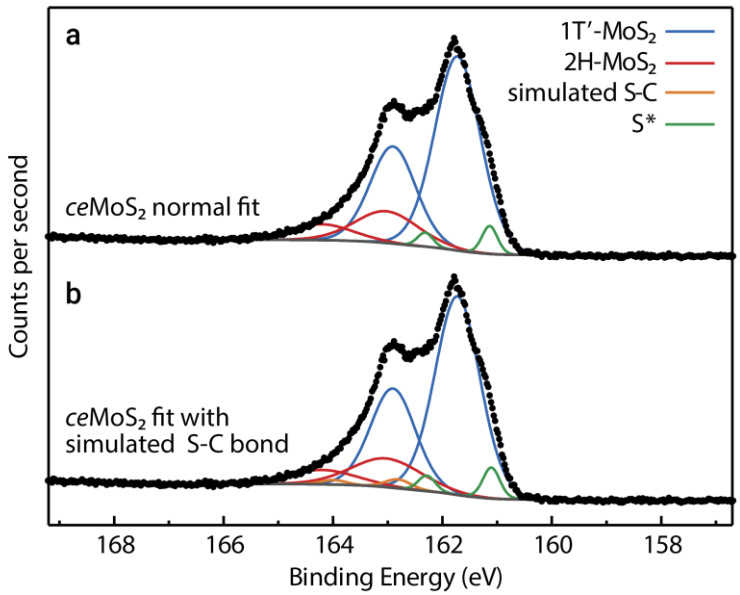

Figure S9. High-resolution XPS of S 2*p* for exfoliated MoS_2 with two types of peak fitting. (a) Three sets of S 2*p* doublet peaks: one doublet for 1T′-MoS_2, one for 2H-MoS_2, and one for sulfur defects. This peak fitting was used to determine the percentage of sulfur in the 2H phase in *ce*MoS_2. The percentage of 2H-MoS_2 for all functionalized samples was constrained based on this fitting. (b) Four sets of S 2*p* peaks, the fourth (simulated S–C) constrained to have the same binding energy relative to the 1T′-MoS_2 peak as the functionalized S–C peak observed in fct-MoS_2 samples. This peak fitting was used to determine the error associated with peak fitting when using peak areas for coverage quantification (left-most bar in Figure 4 of main text).

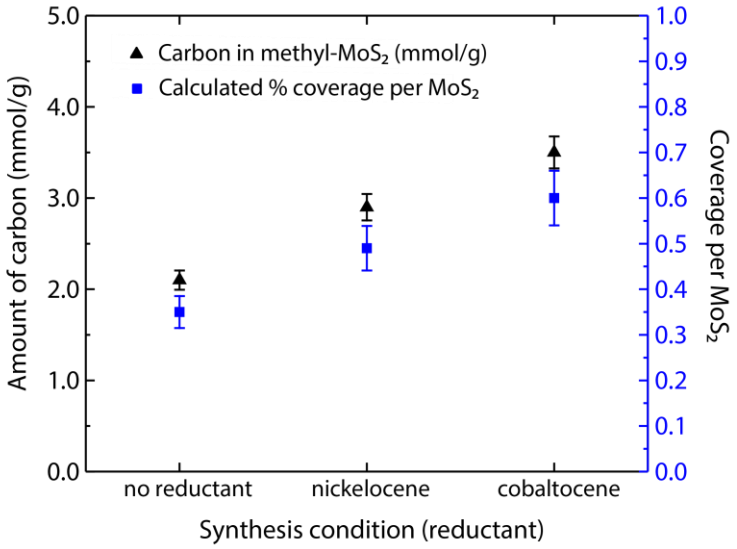

Figure S10. ^{13}C MAS NMR of ^{13}C-methyl-MoS_2 functionalized under three conditions: without reductant, with nickelocene, and with cobaltocene. This technique is semi-quantitative and shows the trend of increasing coverage. Error bars indicate ±10% based on 5% error of external standard and conservative estimate of 5% error from peak fitting.

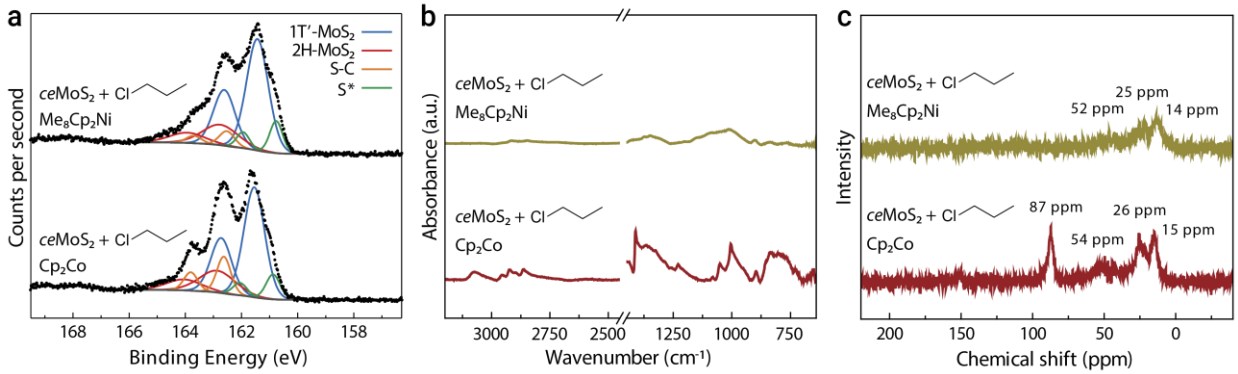

Figure S11. (a) High-resolution XPS of S 2*p* region, (b) ATR-FTIR, and (c) ^{13}C CPMAS NMR data for the functionalization of *ce*MoS_2 with chloropropane in the presence of either octamethylnickelocene (Me_8Cp_2Ni) or cobaltocene (Cp_2Co).

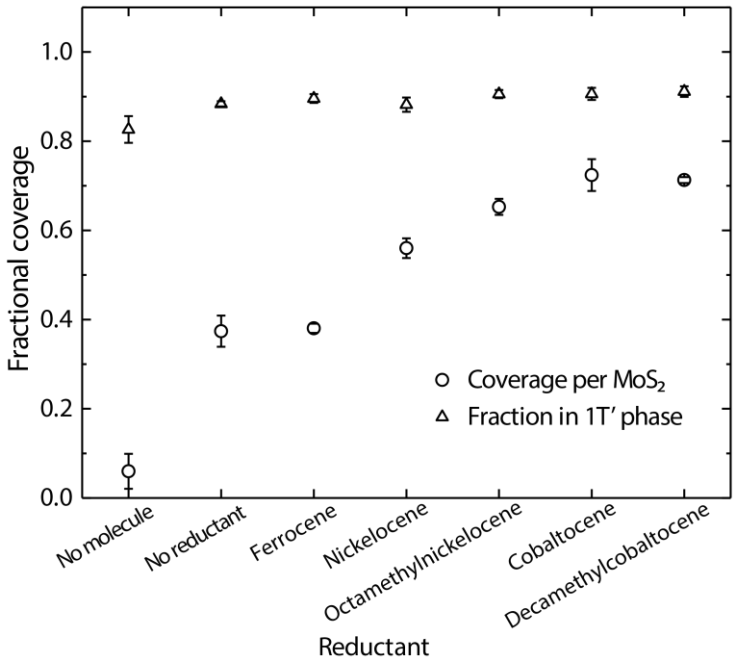

Figure S12. Methyl coverage for methyl-MoS_2 synthesized using iodomethane as a function of the reductant used, and the fraction of MoS_2 in the 1T′ phase based on the S 2*p* XPS peaks. Coverage data are the same as in Figure 4, except with the addition of decamethylcobaltocene ($Me_{10}Cp_2Co$). Although the latter has a more negative reduction potential than cobaltocene, these results indicate that the coverage does not continue to increase as the reduction potential becomes increasingly negative relative to a limiting value. In addition, the fraction of sulfur in the 1T′ phase is consistently ~ 90% in all cases, suggesting that the variation in methyl coverage is not primarily due to the fraction of 1T′ phase. Error bars indicate the standard deviation of at least three samples.

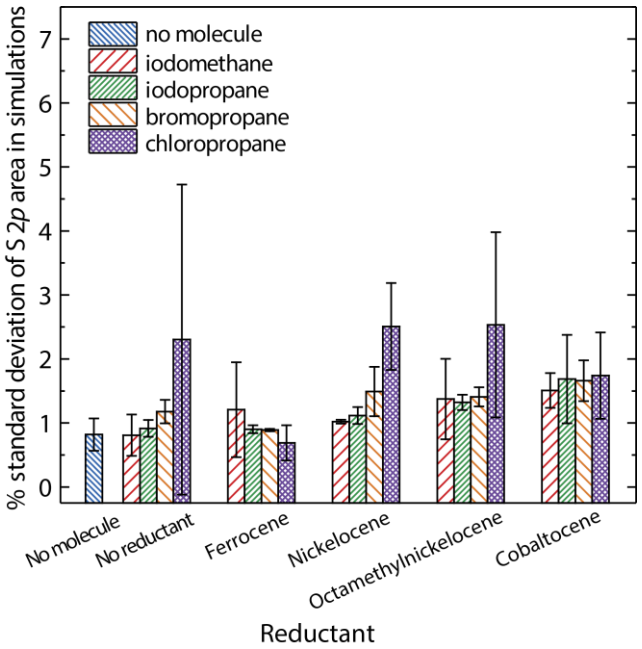

Figure S13. Standard deviations in percentage (%std) of the functionalized S 2*p* peak areas fitted during Monte Carlo simulations (n = 400) for the data presented in Figure 4. Error bars are the standard deviations for the %std. Note that the mean for the %std are below 2% except for conditions involving chloropropane and minimal functionalization, where a larger % error is expected.

V. Tables

Table S1: List of all vibrational frequencies calculated using density functional theory (B3LYP with basis set 6-311G**) for methanethiol and propanethiol, assigned to experimental peaks from methyl-MoS_2 and propyl-MoS_2 (synthesized using iodomethane and 1-iodopropane, respectively). A description is provided for characteristic (experimental) or high-intensity (theoretical) peaks. Calculated frequencies that contained substantial contribution from the S–H bond were not used to assign peaks due the absence of this bond in experimental samples.

	DFT Vibrational Frequency (cm^{-1})	**DFT Intensity (km/mol)**	**Experimental Peak Frequency from MoS_2-CH_3 and MoS_2-$(CH_2)_2CH_3$ (cm^{-1})**	**Description**
Methanethiol	24500	16.1	--	--
	688.57	2.56	694	C–S stretch
	800.70	1.044	--	--
	978.82	11.6	946	C–H in-plane rock
	1099.55	20.8	--	CH_3/S–H rock
	1369.87	10.4	1289	C–H symmetrical wag (CH_3)
	1475.65	5.49	--	--
	1486.35	8.65	--	--
	2659.60	8.76	--	S–H stretch
	3047.06	28.6	2905	C–H symmetrical stretch (CH_3)
	3130.39	10.8	--	--
	3135.79	8.24	--	--
Propanethiol	108.54	4.44	--	--
	174.96	17.7	--	--
	231.84	2.22	--	--
	249.30	0.0700	--	--
	355.97	0.528	--	--
	721.89	3.44	727	C–S stretch
	768.36	4.94	793	C–H in-plane rock (CH_3/CH_2)
	847.50	3.66	--	S–H bend
	882.49	0.334	--	--
	944.17	1.581	898	C–H out-of-plane wag (CH_3/CH_2)
	1043.98	0.0873	--	--
	1074.90	5.08	1054	C–H twist (CH_2/CH_3)
	1135.96	5.40	1082	C–C–C symmetric stretch
	1250.33	0.960	--	--
	1283.66	37.2	1257	C–H wag (CH_2)
	1334.70	3.45	--	--
	1383.15	4.97	--	--
	1418.79	2.79	--	--
	1491.30	2.52	--	--
	1499.35	1.56	--	--
	1502.66	8.80	--	--
	1511.67	5.58	--	--
	2662.37	9.01	--	S–H stretch
	3020.12	22.4	2862	C–H symmetric stretch (CH_3)
	3023.59	11.0	--	--
	3043.41	40.4	2924	C–H symmetric stretch (CH_2)
	3050.68	1.07	--	--
	3081.84	17.6	--	--
	3091.20	36.7	2955	C–H asymmetric stretch (CH_3)
	3098.89	50.4		C–H asymmetric stretch (CH_2/CH_3)

Table S2: The standard reduction potential for each redox couple, the effective reduction potential assuming 50:1 ratio of reductant to oxidant, and the potential on an absolute energy scale using $E(Fc^{+/0})$ = 0.74 V vs SHE (standard hydrogen electrode) and E_{vac} = -4.44 V vs SHE (see supplementary section III.4).

Reductant (A^-)	**Standard Reduction Potential for (A/A^-) vs $E(Fc^{+/0})$ (V)**	**Effective Reduction Potential, 50:1 reductant to oxidant vs $E(Fc^{+/0})$ (V)**	**Potential vs E_{vac} (V)**
ferrocene, Cp_2Fe	0	-0.10	5.08
nickelocene, Cp_2Ni	-0.42	-0.52	4.66
octamethylnickelocene, Me_8Cp_2Ni	-0.95	-1.05	4.13
cobaltocene, Cp_2Co	-1.16	-1.26	3.92
decamethylcobaltocene, $Me_{10}Cp_2Co$	-1.77	-1.87	3.31

VI. References

(1) Baltrusaitis, J.; Mendoza-Sanchez, B.; Fernandez, V.; Veenstra, R.; Dukstiene, N.; Roberts, A.; Fairley, N. Generalized molybdenum oxide surface chemical state XPS determination via informed amorphous sample model. *Applied Surface Science* **2015,** *326,* 151-161.

(2) Grimm, R. L.; Bierman, M. J.; O'Leary, L. E.; Strandwitz, N. C.; Brunschwig, B. S.; Lewis, N. S. Comparison of the Photoelectrochemical Behavior of H-Terminated and Methyl-Terminated Si(111) Surfaces in Contact with a Series of One-Electron, Outer-Sphere Redox Couples in CH_3CN. *J. Phys. Chem. C* **2012,** *116*, 23569-23576.

(3) Noviandri, I.; Brown, K. N.; Fleming, D. S.; Gulyas, P. T.; Lay, P. A.; Masters, A. F.; Phillips, L. The Decamethylferrocenium/Decamethylferrocene Redox Couple: A Superior Redox Standard to the Ferrocenium/Ferrocene Redox Couple for Studying Solvent Effects on the Thermodynamics of Electron Transfer. *J. Phys. Chem. B* **1999,** *103*, 6713-6722.

(4) Voudouris, P. C.; Melfos, V.; Spry, P. G.; Bindi, L.; Kartal, T.; Arikas, K.; Moritz, R.; Ortelli, M. Rhenium-rich Molybdenite and Rheniite in the Pagoni Rachi Mo–Cu–Te–Ag–Au Prospect, Northern Greece: Implications for the Re Geochemistry of Porphyry-style Cu–Mo and Mo Mineralization. *The Canadian Mineralogist* **2009,** *47*, 1013-1036.

(5) Calandra, M. Chemically exfoliated single-layer MoS_2: Stability, lattice dynamics, and catalytic adsorption from first principles. *Phys. Rev. B* **2013,** *88*, 245428.

(6) Qu, Y.; Pan, H.; Kwok, C. T. Hydrogenation-controlled phase transition on two-dimensional transition metal dichalcogenides and their unique physical and catalytic properties. *Sci. Rep.* **2016,** *6*, 34186.

(7) Voiry, D.; Goswami, A.; Kappera, R.; Silva, C. d. C. C. e.; Kaplan, D.; Fujita, T.; Chen, M.; Asefa, T.; Chhowalla, M. Covalent functionalization of monolayered transition metal dichalcogenides by phase engineering. *Nat. Chem.* **2015,** *7*, 45-49.

(8) Eda, G.; Yamaguchi, H.; Voiry, D.; Fujita, T.; Chen, M.; Chhowalla, M. Photoluminescence from chemically exfoliated MoS_2. *Nano Lett.* **2011,** *11*, 5111-5116.

(9) Chou, S. S.; Sai, N.; Lu, P.; Coker, E. N.; Liu, S.; Artyushkova, K.; Luk, T. S.; Kaehr, B.; Brinker, C. J. Understanding catalysis in a multiphasic two-dimensional transition metal dichalcogenide. *Nat. Commun.* **2015,** *6*, 8311.

(10) Fan, X.-L.; Yang, Y.; Xiao, P.; Lau, W.-M. Site-specific catalytic activity in exfoliated MoS_2 single-layer polytypes for hydrogen evolution: basal plane and edges. *J. Mater. Chem. A* **2014,** *2*, 20545-20551.